Solid State Ionics 296 (2016) 137–145

Contents lists available at ScienceDirect

Solid State Ionics

journal homepage: www.elsevier.com/locate/ssi

Statistical analysis of UH_3 initiation using electron back-scattered diffraction (EBSD)

A. Banos *, T.B. Scott

University of Bristol, Interface Analysis Centre, School of Physics, HH Wills Physics Laboratory, Tyndall Avenue, Bristol BS8 1TL, United Kingdom

ARTICLE INFO

Article history:
Received 29 June 2016
Received in revised form 8 September 2016
Accepted 14 September 2016
Available online xxxx

ABSTRACT

Statistical analysis of uranium-hydride (UH_3) initiation location was undertaken on an as-received Magnox-U sample using electron back-scattered diffraction (EBSD). Secondary ion mass spectrometry (SIMS) and focused ion beam (FIB) milling were used for UH_3 identification and complementary examination of the reacted surface. From the interrogation of 147 hydride sites on the electrochemically etched sample it was found that hydride formation occurred predominantly around grain and twin boundaries. Clear preference of hydride attack was observed around grains with high rotational mismatch.

1. Introduction

Uranium-hydride (UH_3) is an air-unstable and pyrophoric substance [1,2] recognised to potentially form as a corrosion product of wet oxidation [3]. The detrimental effects of radionuclide release that could be caused by UH_3 ignition when exposed to air raises safety and technical concerns for various nuclear industry processes. Hydrogen (H_2) is observed to attack uranium metal surfaces in discrete regions (low energy sites) where physi-sorption, dissociation and diffusion are considered to be easier and more favourable [4]. The uranium and hydrogen reaction can be divided into four distinct stages: 1) an induction period where initial hydrogen adsorption and transport through the oxide occurs; 2) a nucleation and growth period where discrete UH_3 sites begin to form and grow; 3) a bulk reaction where coalescence of the hydride sites results in a homogeneous reaction front moving into the surface and 4) a termination period where complete transformation of the metal to UH_3 is achieved.

In this paper the focus is on the early accelerating stage of the reaction where discrete hydride sites begin to nucleate on the surface. Specifically, we examine how metal microstructure controls the location of UH_3 initiation and growth. It is a generally accepted view that the location for hydride nucleation is influenced by a number of parameters. Increasing oxide thickness was found to diminish the nucleation number density and result to UH_3 attack mainly around carbide inclusions and grain boundaries where the oxide is disrupted [5]. Oxide discontinuities can arise as a result of stress relief and termination around the margins of inclusions and across boundaries between grains with different oxidation rates [5]. Hydrogen ingress around these sites is considered faster [6], thus these locations are regarded as preferred for the nucleation of hydride growths. It was also reported that the number density of nucleation sites is diminished by surface and gas impurities as a result of the competition between hydrogen atoms and other impurity entities such as O_2, H_2O, N_2, CO_2 etc. on potential sorption sites [7,8]. Temperature of reaction may also affects the location of the hydrides [9] with the work of Scott et al. [6] showing that on a high temperature regime (≥240 °C) the hydrides formed chains, instead of individual spots, progressing across the margins of high angle grain and twin boundaries. Additionally, the state of the reactive surface prior to hydriding was also observed to affect the hydride size, morphology, location and overall corrosion behaviour of the metal [10].

In addition to these other parameters, the microstructural characteristics of the metal surface play arguably the most vital role in influencing the nucleation number density and location of hydride initiation sites [5]. It is common that the characteristics of the metal surface are reflected in the growing oxide which overlies it. Therefore, it is expected that microstructural deformations like slips and twin boundaries should promote as discontinuities in the oxide surface [5,6]. Grain and twin boundaries [6,11–14] along with inclusions [4,5,13–16] have repeatedly been identified as regions where initial H_2 attack occurs. Though, it is the complex interplay of all the above mentioned factors which still requires better mechanistic understanding.

The difference of this study compared to those previously is that hydride initiation was approached in a more quantitative way, with interrogation of large numbers of growth sites on the same partially hydrided surface, using electron back-scattered diffraction (EBSD). Such an analytical approach permits statistical analysis of hydride growth site locations for natural uranium containing chiefly Fe, Al and C impurities.

* Corresponding author.
E-mail addresses: antonis.banos@bristol.ac.uk, antonisbanos@gmail.com (A. Banos).

http://dx.doi.org/10.1016/j.ssi.2016.09.018

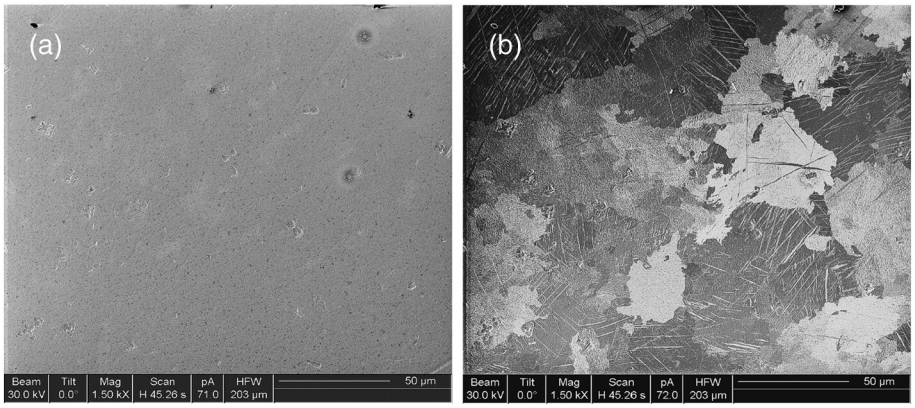

Fig. 1. Focused ion beam (FIB) image of the Magnox-U surface after (a) final polishing and (b) after ion-rastering for 12 min. UC, UC_2 and UCN inclusions of various shapes and sizes may be seen on the former (a) and the metal microstructure in the latter (b) image.

2. Experimental

2.1. Sample

Non-irradiated natural uranium cut from fuel rods and prepared for Magnox reactors was used for this study [10]. The typical method of producing the fuel rod was to cast and β-quench the metal rods from 660 to 700 °C to produce a randomly oriented grain structure. The sample exhibited a high carbon content with an average of 1105 inclusions per mm^2 (Fig. 1a) [10]. Inclusions, usually carbides and carbonitrides, cuboid and rectangular in shape, varied between 3 and 18 μm in maximum dimension. The anisotropic thermal properties of uranium combined with the manufacturing process induce considerable internal stresses within the material evidenced by a multitude of slip planes and twin boundaries (Fig. 1b). A rectangular sample with a surface area of 0.195 cm^2 (0.172 g) was cut from a parent rod, also inducing some further localised strain from mechanical disruption by the action of the Accutom blade at the sample edges.

2.2. Surface preparation

After cutting, the sample was mechanically polished in an open laboratory using water as a lubricant. All sides were polished using silicon-carbon (SiC) papers of increasing level grade up to P4000 (2–3 μm) and then the side of interest received a further polish up to 1/4-μm finish to minimize any residual polishing damage on the surface. Subsequently, the sample was electrochemically polished using a solution containing a 10:6:6 (volume ratio) mixture of ethylene glycol, orthophosphoric acid and absolute ethanol with an applied voltage of 9–10 V and a flowing current of ~0.11 A. The sample was then washed with ultra-pure methanol to remove any residual surface impurities before moved to any instrument for primary examination. Gentle cleaning preparation was vital for the experiment as a pristine surface, devoid of polishing (strain) damage, and was necessary for the analysis. The sample was then directed to a FEI FIB201 focused gallium ion beam instrument for preliminary examination. Prior to EBSD analysis, further fining of the surface was done regionally, using ion-sputtering with a high beam current (6600 pA) at a grazing angle of 5–10° with respect to the inspected surface.

2.3. Preliminary examination

It is known that on electropolished samples the microstructure is revealed when ion bombardment is used to clean the oxide from the surface. Fig. 1 shows the sample surface before and after FIB-rastering for 12 min with a high current incident beam. The Magnox-U reveals an intricate microstructural texture with a linear variation in grain size, exhibiting grains from ~2 μm to as high as >56 μm in size. Certain grains contained significant numbers of twin boundaries and slip planes. Twinning modes are displayed as elongated ribbon like structures up to several microns in width, with the most predominant to be the {130}⟨310⟩ and '{172}'⟨312⟩ systems. The former is a compound twin and the latter is a Type 2 twin and both exhibit a high angle of misorientation with the parent grain at ~69° and ~92.70°, respectively [12]. EBSD analysis on the material (Fig. 2a) showed a random and complex grain structure with a wide spread of angular misorientation between the grains. Textural features within the grains indicate plastic deformation as a result of compressing or stressing forces developed during fabrication. Alpha-U was confirmed to be the exclusive metallic phase along with UC and UC_2 phases that were also spotted (Fig. 2b).

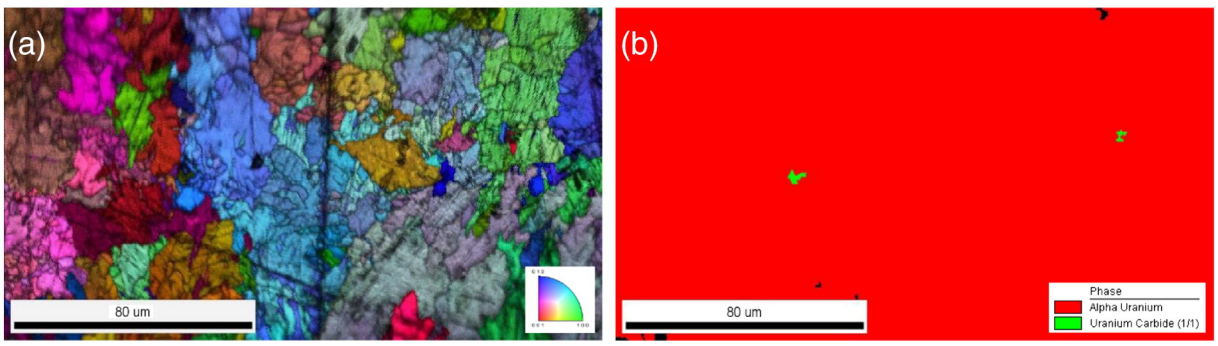

Fig. 2. Illustrating (a) a crystallographic orientation map and (b) a phase map of the Magnox-U surface before the hydriding process. Grain orientation anisotropy along with a highly textured surface may be observed on (a). The primary phase is alpha-U (highlighted in red) along with UC (bright green) and UC_2 been also identified using secondary ion mass spectrometry (SIMS). (For interpretation of the references to colour in this figure legend, the reader is referred to the web version of this article.)

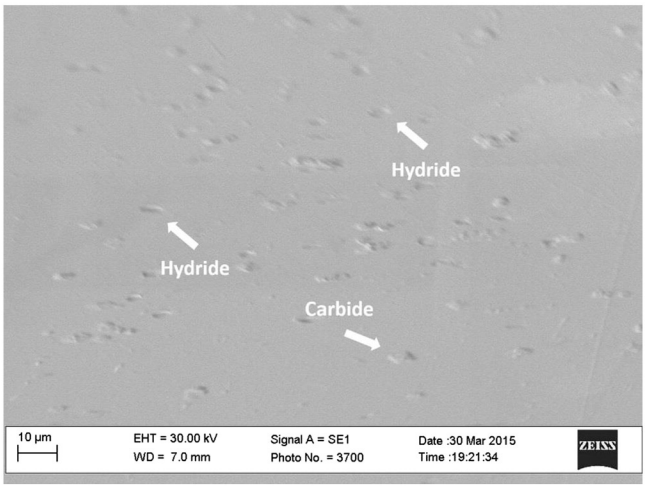

Fig. 3. Secondary electron (SE) image of the hydrided surface. Hydride sites appear as micron-scale blister-like spots while carbide inclusion sites of various shapes are also identified.

2.4. Hydriding reaction

After primary characterization, the sample was left exposed in air for 30 min (total exposure 40 min) to ensure that oxide development has reached the linear oxidation rate stage. An oxide with an average thickness of ~20 nm was expected on the surface [9]. The sample was then loaded in a stainless steel reaction cell and evacuated to $<1 \times 10^{-6}$ mbar. The temperature was raised to 180 °C and left to stabilize for 3 h. This period was considered long enough for most of the oxide impurities to diffuse out but short enough for no measurable oxide transformation [17] or metal grain growth [18] to occur. Deuterium (D_2) was chosen to be the reacting gas instead of hydrogen as isotopic labelling allowed for easier tracing the hydride/ deuteride growths when using secondary ion mass spectrometry (SIMS) to map the sample surfaces. D_2 is chemically identical to H_2 in terms of hydride formation behaviour and hence for the rest of this paper terms such as hydride/ hydriding may refer to deuteride/deuteriding. 500 mbar of D_2 was introduced to the fixed volume. A slight (<0.5 mbar) decrease in pressure was observed seconds after D_2 introduction and was ascribed to gas diffusion into the surface oxide. After 4 min, a measureable, continuous drop in gas pressure was observed signifying the onset of hydride nucleation. The reaction was immediately ceased after a pressure drop of 1 mbar was recorded, achieved by pumping the reacting gas from the system. The observed pressure drop was equivalent to 0.00194 mmol of consumed D_2 to form UD_3, which was considered ideal for the scope of the experiment. Here, we need to note that the temperature was set to stabilize on a regime where the reaction rate (even on the accelerating stage) was moderate enough to control and limit the reaction, therefore the selected reaction temperature was far from arbitrary.

3. Analysis techniques

3.1. Secondary ion mass spectrometry (SIMS)

To determine if hydride formation had successfully occurred on the metal surface SIMS was used to produce ion mass maps of the surface. A custom made SIMS instrument, consisting of a FEI focused gallium ion source fitted to a Vacuum Generators model 7035 double-focusing magnetic sector mass analyzer was employed for the examination [10]. The analysis was conducted using a beam current of 3 nA on positive ion mode. Peak fitting of the mass spectrum for uranium along with uranium-hydride (UH^+) and uranium-deuteride (UD^+) fragments was necessary for the scopes of the experiment as it was imperative to establish that these centers were indeed hydride growths before any further examination takes place. The hydrides were identified by obtaining ion maps at the identified and corresponded masses (239 and 240 amu for the UH^+ and UD^+ signal, respectively). The oxide layer thickness was measured using depth profiling of U^+ and uranium-dioxide (UO_2^+) ion clusters. Depth profiling was also used to confirm the existence of hydrides in between the metal-oxide interface.

3.2. Focus ion beam (FIB) milling and rastering

Preliminary and post-hydriding examination of the surface was conducted using a FEI FIB-201 focused gallium ion beam instrument [10]. Ion beam milling was used to raster the thin oxide surface of the electrochemically etched sample and reveals the metal microstructure. To achieve this, the source was adjusted such that the angle between the incident beam and the surface was 5–10° and ion-sputtering was completed on certain regions prior to EBSD analysis. The sputtering depth was selected to be 100 nm just so that the thin oxide layer was wiped off and any residual surface strain in the metal was also removed. The

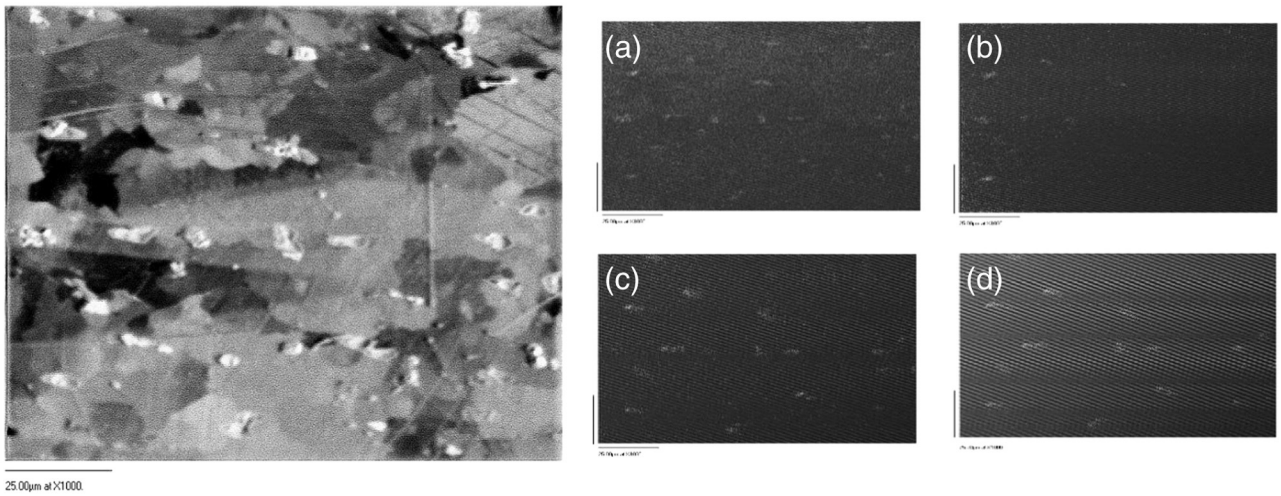

Fig. 4. SE image of the partially hydrided surface with inset ion maps for (a) U^+ (b) UO_2^+ (c) UH^+ and (d) UD^+ ion clusters. It is clear that regions of enhanced ion yield (brighter areas) are coincident for the UH^+ and UD^+ ion maps.

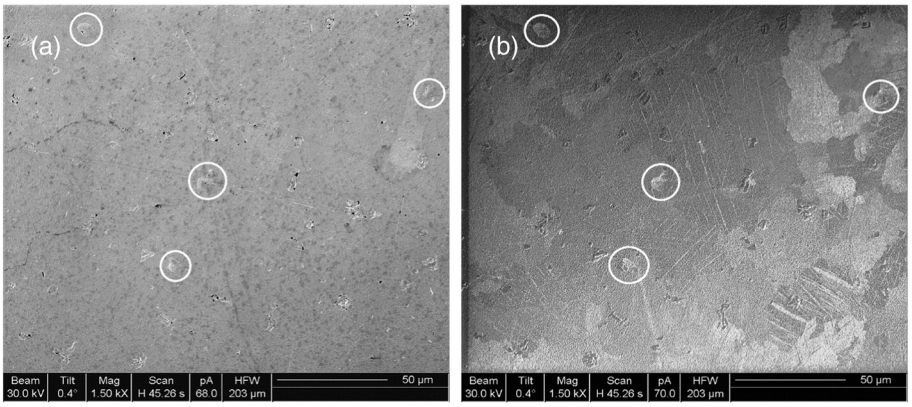

Fig. 5. Focused ion beam (FIB) image of the hydrided uranium surface (a) before and (b) after ion-rastering for 12 min to remove the surface oxide. Circled areas denote identified hydride growth sites. It is clear that preferred nucleation occurred around grain boundaries, deformation twins and particle inclusions.

same procedure was followed prior to and after the surface was partially hydrided.

3.3. Electron back-scattered diffraction (EBSD)-secondary electron (SE) imaging

The sample was then quickly directed to a ZEISS EVO-MA10 scanning electron microscopy (SEM) instrument with a LaB_6 source, an accelerating voltage of 30 kV and a probe current of 0.7 nA [10]. EBSD analysis was performed using a Digiview 3 high speed camera and an EDAX-EBSD instrumentation fitted with the orientation imaging microscopy (OIM) Analysis 6.2 software for data collection and processing. Crystallographic orientation maps were obtained prior to and after the hydriding reaction took place on the surface.

4. Results

4.1. SEM analysis

The hydriding reaction was deliberately ceased after only 0.00194 mmol of D_2 had reacted with the metal. This small quantity of gas consumption was ideal to ensure the reaction was halted in the very early stages of nucleation and growth. Initial observations by SEM showed significant hydride attack at the edges of the sample and at regions across the surface where pre-existing surface damage was apparent. Only three large hydride pits (>100 µm) were identified across the whole surface, with all remaining hydrides developing as small diameter growth spots (Fig. 3). These small blister-type hydrides exhibited a diameter between 4 and 8 µm which had not breached the overlying oxide. The nucleation density was estimated around 115–215 hydrides/ mm^2. The hydride sites did not appear to be directly associated with carbide inclusions. Only a very small number were observed to form around inclusions, however with SEM inspection alone it was impossible to ascertain if the hydrides had formed preferentially at the inclusion sites or also coincided with grain and twin boundaries. The phenomenon of inactivation of inclusion sites for hydride nucleation when the surface is electrochemically etched has also been confirmed by Harker et al. [19] and ascribed to formation of oxide at the carbide-metal interface making hydrogen ingress less favourable around these sites.

4.2. SIMS analysis - UH_3 identification

SIMS allowed quick verification and location of hydride spots across the corroded uranium surface. By obtaining mass ion maps across areas where a hydride was suspected to form we were able to identify and quantify the size and number of hydrides. Fig. 4a depicts a SE image of the hydrided surface with the inset mass ion maps (a–d) displaying the various phases for the same area. For the UH^+ and UD^+ ion maps (Fig. 4c, d), it is evident that the areas of enhanced signal intensity coincide, confirming the existence of hydride nucleation and growth sites. SE imaging combined with mass ion maps led to a more accurate and safe estimation of the hydride nucleation density, as identification and quantification of the hydrides was facilitated by both analysis techniques.

4.3. FIB examination

The significant advantage of investigating electrochemically etched samples is the absence of a work-hardened layer which is ubiquitous on mechanically polished surfaces. If the surface is pristine, then by using direct ion-sputtering the protective oxide can be removed and the microstructural characteristics of the metal surface can be revealed. By doing this on a partially hydrided surface direct insight to the preferential location of hydride growth could be gained. Fig. 5 displays a selected area of the hydrided uranium surface (a) before and (b) after ion-sputtering. Texture, morphology and hydride location can be easily identified using this technique, however it must be understood that such an analytical approach is semi-quantitative in terms of hydride initiation location. The reason for this is that the hydrided surface cannot be characterized using the FIB, therefore information about crystal orientations, types of deformation and angle of misorientation between the grains cannot be directly correlated with the hydride location. This problem was overcome by using EBSD. Prior to analysis, the hydrided

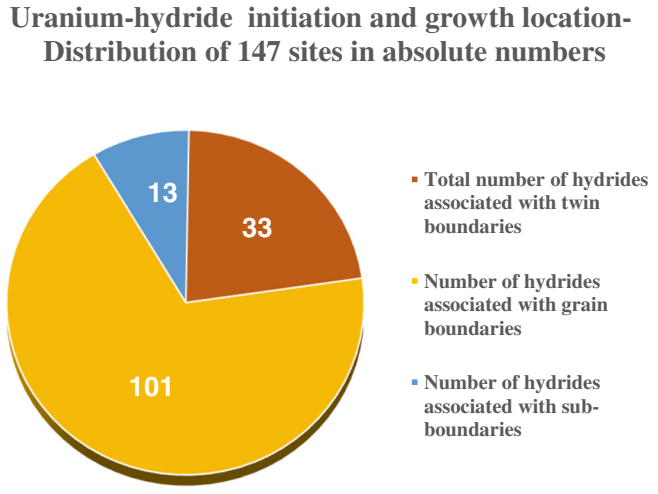

Fig. 6. Categorisation of uranium-hydride (UH_3) initiation and growth location for a total of 147 sites.

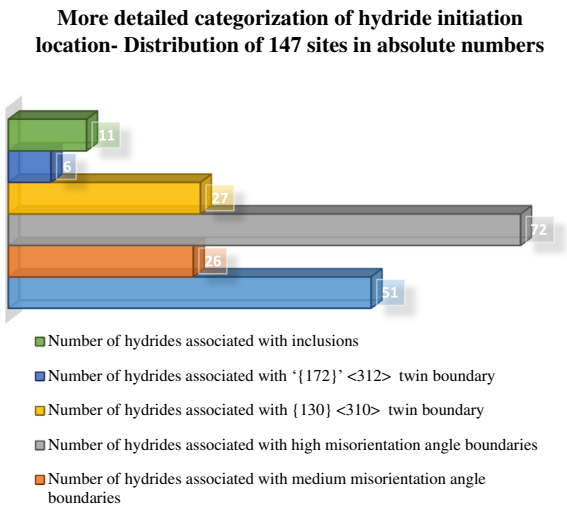

Fig. 7. Showing the absolute number of hydrides associated with various features on the metal microstructure. It is important to note that the sum of the displayed values exceeds the total of 147 hydride sites since multiple features may be assigned as initiation points for a single hydride site.

surface underwent further preparation using ion-sputtering at a very low angle (see Surface preparation section). The sputtering depth (0.1 μm) was carefully chosen so that it did not exceed the depth of the hydride nuclei but removed the surface oxide.

4.4. EBSD examination

EBSD facilitated direct post-mortem measurement of the characteristics of the uranium microstructure associated with hydride nucleation. For example EBSD enabled the quantification of the crystallographic orientations of the grains, including the identification of twin boundaries and the angle of misorientation between them. The angle of rotational mismatch between the neighbouring grains was shown exert significant control on hydride initiation location [6,14]. Such an investigation has never previously been performed on a Magnox-U sample.

The grain/twin boundaries were divided into three groups with respect to the observed misorientation angle as follows:

i. Low misorientation angle (LMA) boundaries (2–15°)
ii. Medium misorientation angle (MMA) boundaries (15–65°)
iii. High misorientation angle (HMA) boundaries (65–180°)

It is important here to note that the {130} ⟨310⟩ and '{172}' ⟨312⟩ systems which are the main twinning modes for alpha-U were included in the HMA group as they exhibit a high angle of misorientation with the parent grain at 69° and 92.7°, respectively. Twinning modes and grain boundaries of all three groups were discreet when hydride initiation location was determined. A total of 0.2965 mm^2 of the hydrided uranium surface was successfully EBSD-mapped. From a total of ~80 mm length of boundary interface, LMA boundaries were found to dominate the surface, measuring 2.7 times the length of HMA boundaries.

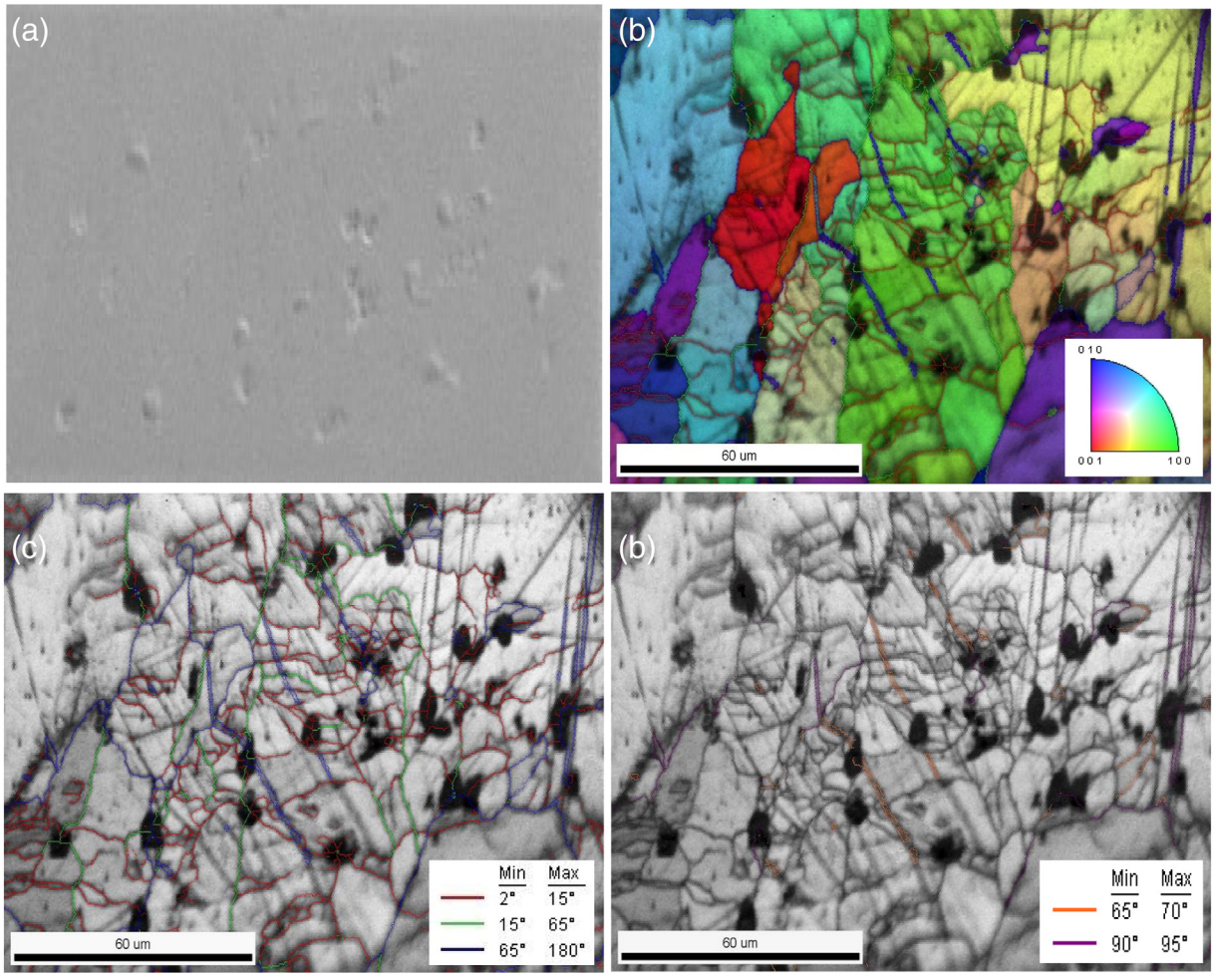

Fig. 8. A series of electron back-scattered diffraction (EBSD) maps from a region of the hydrided uranium surface showing (a) a SE image (b) a crystallographic orientation map (c) a misorientation boundary map and (d) a twin boundary map.

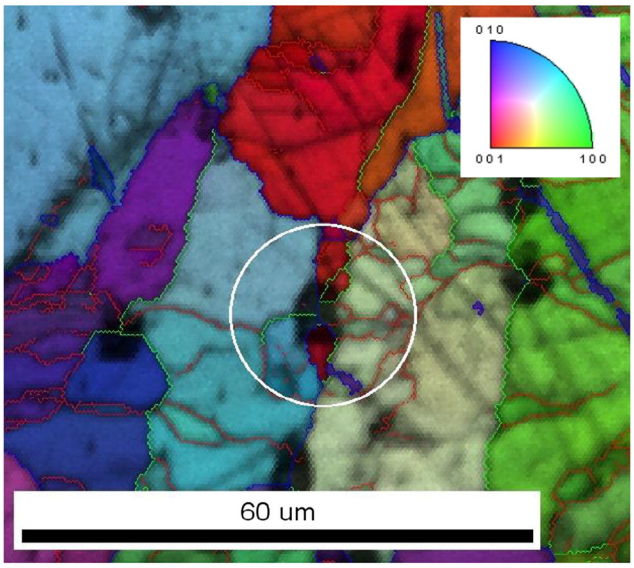

Fig. 9. A crystallographic orientation map showing a hydride growth site at an intersection between a medium and high misorientation angle boundary (white circled area). Low misorientation angle (LMA) boundaries are also crossing the margins of the growth centre.

In the analysed area a total of 147 hydrides were interrogated. However, simple derivation of the spatial nucleation density (hydrides/mm^2) using the previously mentioned values (147 hydrides, 0.2965 mm^2) would be erroneous as the attack across the surface was not perfectly homogeneous, while selective and site specific EBSD scans have been conducted for the scopes of the experiment. SEM imaging and SIMS hydride identification assisted the determination of the hydride nucleation and growth sites to ensure that no misjudgement between a hydride and an inclusion site could be made during EBSD analysis. After UH_3 identification was established, hydride initiation location relative to metal microstructure was determined. The UH_3 sites were fitted into nine categories associated with:

i. LMA boundaries
ii. MMA boundaries
iii. HMA boundaries
iv. {130} ⟨310⟩ twin system
v. '{172}' ⟨312⟩ twin system
vi. Inclusions (all types)
vii. Twin boundaries (total number of both twinning modes)
viii. Grain boundaries
ix. Sub-boundaries

It is essential at this point to proceed to some clarifications on how the sites were listed to avoid misinterpretation of the results. Firstly, some of the interrogated sites were found to form at triple point junctions of misoriented boundaries therefore multiple boundary angles were taken into account for one hydride. Boundaries crossing the margins of a hydride were not considered as growth locations. A clear separation between grain boundaries, sub-boundaries and twin boundaries was made (Fig. 6). Inclusions sites were never found to be solely responsible for hydride initiation.

Figs. 6 and 7 consolidate the absolute numbers of hydride nucleation and growth location for all 147 sites. From the analysis it was shown that:

i. UH_3 sites formed almost exclusively around grain and twin boundaries measuring 134 sites, out of the total 147, on these areas (Fig. 8a–d).
ii. Hydrides tended to form on junctions of rotational grain mismatch and where grain multiple boundaries intersected (Fig. 9) e.g. triple point junctions.
iii. A clear preference for nucleation at high misorientation angle boundaries (including dislocations) was observed. Table 1 displays the theoretical values of distance between two hydride centers across a boundary, assuming equidistant sites, calculated for all three angle boundary groups. Only 51 hydrides were identified in a total length of 51 mm for LMA boundaries while on the HMA boundaries (including the twin boundary locations) 105 hydrides in a length of ~19 mm were observed (Table 1). Assuming the same average distance between two hydrides on the boundary, the frequency in which a hydride was met in the HMA boundary was 2.17 and 5.56 times greater compared to that of the MMA and LMA boundaries, respectively. Scott et al. [6] also observed this phenomenon and ascribed this behaviour to the difference on the effective width of the grain boundaries (zones of disordered material) when exposed at the surface due to variation in rotational angle.
iv. Clear distinction of attack preference between the different twin boundary types cannot be concluded as the {130} ⟨310⟩ compound twin was more abundant with respect to the '{172}' ⟨312⟩ system and accordingly received proportionally greater hydride attack (Fig. 10).
v. Due to the abundance of carbide inclusions on the surface some of the interrogated hydride sites coincided with carbide inclusions. However these sites were not found to be solely responsible for hydride initiation as LMA and HMA junctions were coincident in all cases (Fig. 11).
vi. Areas of the surface that have been ion-sputtered and EBSD mapped prior the hydriding reaction did not undergo any observable hydrogen attack (Fig. 12).

5. Discussion

5.1. Grain and twin boundaries as preferred nucleation locations

The data reinforces the view that hydride initiation location is significantly influenced by the microstructure of the metal surface. Low energy sites and strained regions like twin and grain boundaries are reflected in the overlying oxide as physical discontinuities therefore sites where hydrogen ingress is easier and more favourable. Over 90% of the interrogated sites were associated with grain and twin boundaries, which tallies with numerous previous studies conducted on pure rather than Magnox-U [6,11–14]. It is broadly believed that these sites act as short-circuit paths for H_2 diffusion. Twinning on the metal

Table 1
Theoretical derived values of average distance across the boundary between two hydrides assuming equidistant sites.

	Total misorientation angle boundary length (mm)	Number of hydrides associated with misorientation angle boundary[a]	Average distance across the boundary between two sites
Low (2–15°)	50.98	51	1.00
Medium (15–65°)	10.15	26	0.39
High (65–180°)	18.85[a]	105	0.18

[a] Including both primal twinning modes.

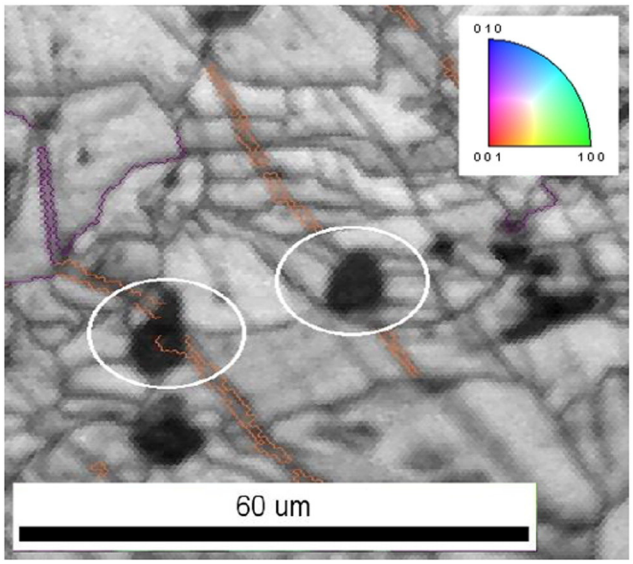

Fig. 10. Illustrating hydrides forming on {130} ⟨310⟩ compound twins.

occurs when one or more lattice cells of the parent structure is sheared due to applied stress and due to plastic deformation results in a new cell at a certain misorientation with the parent grain [20]. Twins were also addressed as preferential hydride initiation locations [5,6,13]. However, there is discrepancy in the literature as to whether nucleation occurs or the diffused H_2 is trapped within the boundary impeding further diffusion [21]. In this work, it was confirmed that hydride nucleation can and does occur on grain and twin boundaries. No clear distinction of attack preference was resolved between the two main twinning modes. From the analysis it was found that the {130} ⟨310⟩ compound twin nucleated more sites (27/147) than the '{172}' ⟨312⟩ system (6/147), however the former was more abundant on the surface.

5.2. High misorientation angle (HMA) boundaries as preferred nucleation locations

Hydrogen attack is more pronounced specifically for boundaries with high crystallographic mismatch between the neighbouring grains. 65° was designated the lower cut off limit for HMA boundaries in order to incorporate the rotational mismatch for both most important types of dislocations, the {130} ⟨310⟩ and '{172}' ⟨312⟩ twin systems (Table 1). Indeed, hydrogen attack along the HMA boundaries was considerably more frequent with respect to the other boundaries. The hydrides also tended to form on junctions of rotational mismatch and where grain multiple boundaries intersected e.g. double or triple point boundary junctions (Fig. 9). Scott et al. [6] also observed this behaviour working on a depleted uranium sample which was mechanically polished and annealed prior to hydriding. They attributed the phenomenon to difference on the exposed boundary width between high and low misorientation angle boundaries. It was inferred that although the width of the disordered boundaries is equivalent in the inner bulk of the metal, the HMA boundaries exhibit a higher width compared to those with lower angles when projected on the surface [6]. If this is true, then HMA boundaries providing larger disordered areas are more likely to be attacked first.

To add another coincident dimension to this argument, it is vital here to explain how inhomogeneous initial oxidation between metal grains of different crystallographic orientation affects the early hydriding behaviour on uranium. It is already established that grains with differed crystal orientation oxidise initially at measurably different rates and this leads to a very uneven oxide thickness across the surface of the metal for the first 40 nm of growth [22]. It follows logically that the higher the rotational mismatch between the neighbouring grains the greater the disparity of oxide thickness between them in the early stage of growth. As further oxidation continues, regions of thinner oxide will in essence catch up those which initially thickened faster. Hence above adjoining surface-exposed metal a mechanical strain will be generated in the forming oxide layer. In Fig. 13, a simplified stepwise schematic of this process is provided with y_A, y_B and y_C representing the oxide thickness over grains A, B and C, respectively as a function of increasing oxidation time ($t_0 \rightarrow t_2$). Taking the comparison between grains B and C as an example, by time t_1, $y_C - y_B \gg 0$ while by time t_2 the relative difference in oxide thickness (y_C vs. y_B) is much smaller, becoming increasingly insignificant with further oxidation. Comparably there is much less by way of oxide growth mismatch between grains A and B due to low rotational mismatch and thus the stress generated in the oxide over the metal grain boundaries is much smaller by comparison. It is suggested that through this mechanism, the grain boundary discontinuity is propagated into the overlying oxide as it forms and may subsequently serve as an extra and coincident phenomenon for facilitating more rapid ingress of H_2 in these zones, leading to preferential attack of the metal surface where crystallographic mismatches between adjoining metal grains are most pronounced.

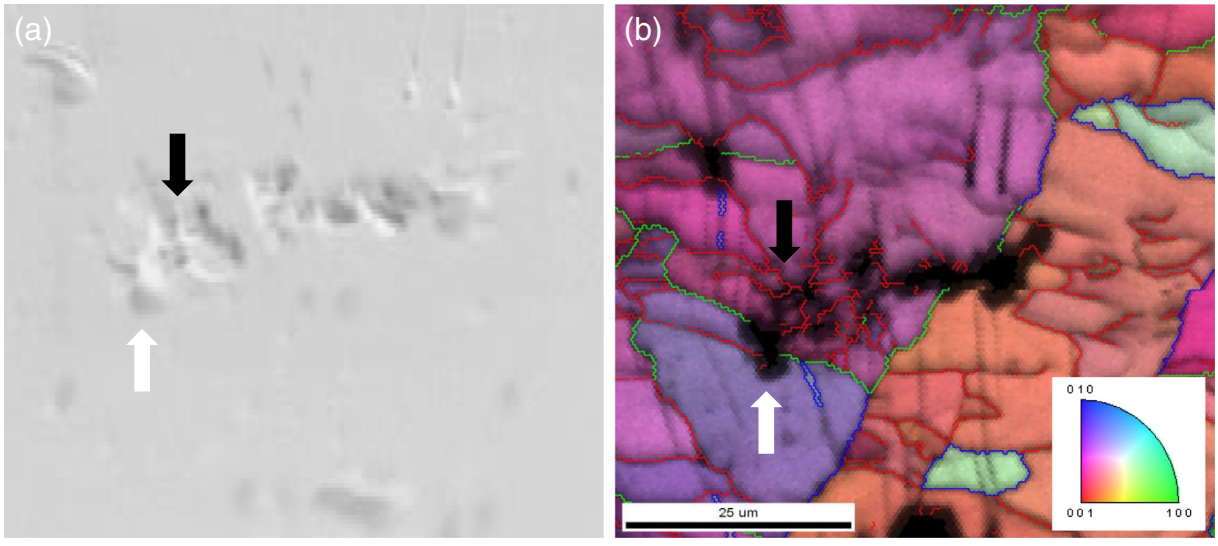

Fig. 11. Showing on (a) a hydride spot (white arrow) nucleating at the margins of a carbide inclusion (black arrow) and on (b) a combined crystal orientation and misorientation boundary map of the same area verifying the contribution of a low misorientation angle (LMA) and medium misorientation angle (MMA) boundary to the hydride location.

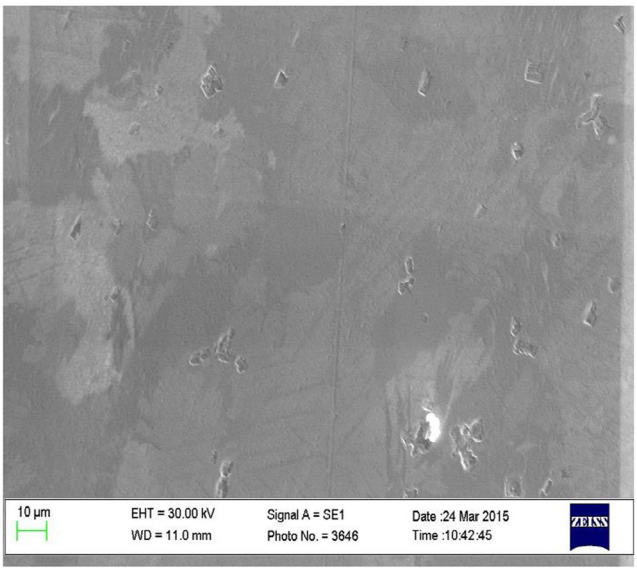

Fig. 12. Illustrating a pre-ion sputtered area of the hydrided sample. The surface has not received any hydrogen attack even though the oxide at this area is thinner compared to other attacked regions. It is assumed that the absence of strain and Ga^+ implantation due to ion-sputtering on the surface left this region intact and non-reacted.

5.3. Inclusions as preferential nucleation sites

It was reported in the literature that inclusions act as perfect sites for nucleation of hydride growth [4,5,13–16], however this deduction was not broadly accepted [12,23]. The higher melting point of carbon impurities with respect to uranium results in induced stresses at the uranium-uranium carbide interface during the fabrication process. This along with the different oxidation rates between the uranium and carbide surface [24] promote lattice oxide distortion on the perimeter of the inclusion. Therefore, it would be expected that inclusions will always be attacked early in the onset of the reaction. However, in this work only 11 out of 147 hydrides were associated with inclusions (<8%). Furthermore, the carbides were never seen to be solely responsible for hydride initiation as LMA and HMA junctions were apparent on these regions. This phenomenon could be regarded as unexpected, especially for a sample with such a carbon impurity content (~1105 carbides/mm^2). However, we attribute the unexpected behaviour to inactivation of carbide sites caused by the electropolishing preparation. Harker et al. [19] showed that the preference for inclusions to act as hydride nucleation sites can be removed by using electropolishing. During electropolishing the overlying oxide seems to penetrate down the surface at the inclusion-metal interface and thus considerably increasing the distance at which hydrogen atoms should travel to reach the metal and eventually nucleate [19]. We are in agreement with this supposition, and have observed very similar hydriding behaviour with respect to hydride characteristics and morphology, albeit on a metal of different provenance.

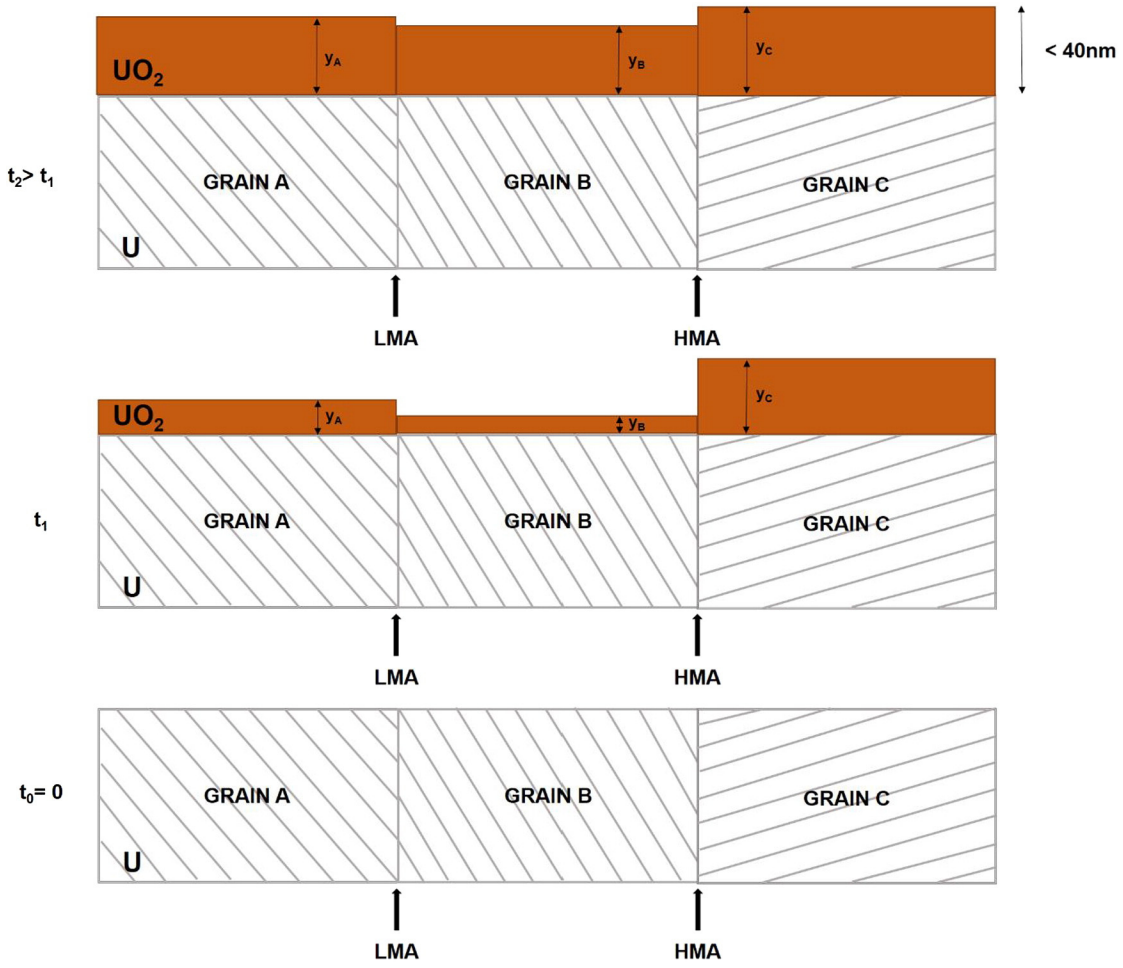

Fig. 13. Schematics showing how the oxidation kinetics progresses on grains with different rotational mismatch and how the differed oxidation rates lead to stress generation on the oxide-oxide interface. LMA and HMA refer to low misorientation angle and high misorientation angle boundaries, respectively.

5.4. Surface passivation due to ion-sputtering

Another interesting observation was the resilience that the pre-ion sputtered surface exhibited to hydrogen corrosion. Areas that have been ion sputtered prior to the hydriding reaction were not attacked suggesting surface passivation had occurred. Fig. 12 displays a pre ion-rastered region of the partially hydrided sample where only carbide inclusions of multiple shapes and sizes can be identified. No phase transformation has been witnessed on these areas. Surface passivation is assumed to occur due residual strain wipe-off and Ga^+ implantation on the surface using ion sputtering. Pristine and strain-free surfaces could possibly interact with H_2 later on the reaction. If such an assumption stands, then the effect of strain on the onset of the hydriding reaction should be examined thoroughly. Additionally Ga^+ deposition could effectively retard the reaction as Ga^+ ions are competing with H_2 on available sorption sites potentially affecting the overall H_2 ingress to the metal.

6. Conclusion

Statistical analysis of UH_3 initiation was undertaken on a Magnox-U sample using EBSD. From the investigation of 147 hydride sites on the electrochemically etched surface it was found that hydride formation occurred predominantly around grain and twin boundaries. Clear preference of hydride attack was observed around grains with high crystallographic mismatch. Further investigation should focus on the effect of mechanical stress caused on the metal by the burn-up of the material and/or stripping off the coating material to corrosion. Research to that direction is critical in order to allow the translation of a large body of research on virgin (unirradiated) uranium to a real-world scenario.

Acknowledgements

The authors would like to thank the RCUK-Engineering & Physical Sciences Research Council (EPSRC) (1338575) and Sellafield Ltd. for funding this project as part of 42-month PhD research studentship (Ref: 1338575), at the Interface Analysis Centre (IAC), School of Physics, University of Bristol. Also, would like to thank Mr. John Jowsey from the Sellafield Centre of Expertise in Uranium and Reactive Metals (URM) for contextual guidance and technical input.

References

[1] F. Le Guyadec, X. Génin, J. Bayle, O. Dugne, A. Duhart-Barone, C. Ablitzer, J. Nucl. Mater. 396 (2) (2010) 294–302.
[2] C. Ablitzer, F. Le Guyadec, J. Raynal, X. Génin, A. Duhart-Barone, J. Nucl. Mater. 432 (1) (2013) 135–145.
[3] M.M. Baker, L. Less, S. Orman, Trans. Faraday Soc. 62 (1966) 2513–2524.
[4] R. Arkush, A. Venkert, M. Aizenshtein, S. Zalkind, D. Moreno, M. Brill, et al., J. Alloys Compd. 244 (1) (1996) 197–205.
[5] D. Moreno, R. Arkush, S. Zalkind, N. Shamir, J. Nucl. Mater. 230 (2) (1996) 181–186.
[6] T.B. Scott, G.C. Allen, I. Findlay, J. Glascott, Philos. Mag. 87 (2) (2007) 177–187.
[7] J. Bloch, D. Brami, A. Kremner, M. Mintz, J. Less Common Met. 139 (2) (1988) 371–383.
[8] D.F. Teter, R.J. Hanrahan, C.J. Wetteland, Uranium Hydride Nucleation Kinetics: Effects of Oxide Thickness and Vacuum Outgassing, Los Alamos National Lab, NM (US), 2001.
[9] S. Bazley, J. Petherbridge, J. Glascott, Solid State Ionics 211 (2012) 1–4.
[10] A. Banos, C.A. Stitt, T.B. Scott, The effect of sample preparation on uranium hydriding. Under submission.
[11] J. Bloch, F. Simca, M. Kroup, A. Stern, D. Shmariahu, M. Mintz, et al., J. Less Common Met. 103 (1) (1984) 163–171.
[12] J. Bingert, R. Hanrahan, R. Field, P. Dickerson, J. Alloys Compd. 365 (1) (2004) 138–148.
[13] M. Hill, R. Schulze, J. Bingert, R. Field, R. McCabe, P. Papin, J. Nucl. Mater. 442 (1) (2013) 106–115.
[14] C.P. Jones, T.B. Scott, J.R. Petherbridge, J. Glascott, Solid State Ionics 231 (2013) 81–86.
[15] L. Owen, R. Scudamore, Corros. Sci. 6 (11) (1966) 461–468.
[16] P. Shi, L. Shen, B. Bai, D. Lang, L. Lu, G. Li, et al., J. Nucl. Mater. 441 (1) (2013) 1–5.
[17] J. Knowles, I. Findlay, D. Geeson, S. Bazley (Eds.), The Influence of Vacuum Annealing on the Nucleation and Growth Kinetics of Uranium Hydride, MRS Proceedings, Cambridge Univ Press, 2012.
[18] J. Bloch, M.H. Mintz, J. Less Common Met. 166 (2) (1990) 241–251.
[19] N. Harker, T. Scott, C. Jones, J. Petherbridge, J. Glascott, Solid State Ionics 241 (2013) 46–52.
[20] A. Crocker, J. Nucl. Mater. 16 (3) (1965) 306–326.
[21] A. Loui, The Hydrogen Corrosion of Uranium: Identification of Underlying Causes and Proposed Mitigation Strategies, Lawrence Livermore National Lab# LLNL-TR-607653, Livermore, 2012.
[22] J. Glascott, Philos. Mag. 94 (3) (2014) 221–241.
[23] R.J. Hanrahan, M.E. Hawley, G.W. Brown (Eds.), The Influence of Surface Morphology and Oxide Microstructure on the Nucleation and Growth of Uranium Hydride on Alpha Uranium, MRS Proceedings, Cambridge Univ Press, 1998.
[24] T. Scott, J. Petherbridge, N. Harker, R.J. Ball, P. Heard, J. Glascott, et al., J. Hazard. Mater. 195 (2011) 115–123.